Journal of Materials Chemistry B

Accepted Manuscript

ROYAL SOCIETY OF CHEMISTRY

rsc.li/materials-b

Journal Name

ARTICLE

Preparation and biological effects of apatite nanosheet-constructed porous ceramics

Received 00th January 20xx,
Accepted 00th January 20xx

DOI: 10.1039/x0xx00000x

www.rsc.org/

Ying Chen,[a] Zhihui Sun,[b] Yanyan Li[b] and Youliang Hong*[a]

The design and processing of bioceramics into specific architectures (especailly have specific architectures at micro-/nanoscale) to improve their biological performances or extend their applications always become the cutting-edge research of bioceramics. Herein, we designed a kind of apatite nanosheet-constructed porous ceramics (AN-PCs), which were fabricated by foam moulding, high heat sintering and then water soaking the α-tricalcium phosphate (/hydroxyapatite -contained porous biphasic calcium phosphate ceramics. Experiments demonstrated that such stereo-nanotopographies had excellent cytocompatibility, and could regulate mesenchymal stem cells (MSCs) to differentiate into osteogenic lineages. And the in vivo ectopic-implant showed that the AN-PCs possessed the osteoinductivity. Thus the AN-PCs reported herein show the improved biological performances to repair the hard tissues.

Introduction

Now accumulating evidences have demonstrated that some specific micro-/nanotopographies, such as disordered pits,[1] pillars,[2] surface oriented nanotubes[3] or nanowires,[4] can mediate the osteogenic differentiation of mesenchymal stem cells (MSCs, sometimes, also referred to as marrow stromal cells[5]). Such finding is very significant for bone tissue engineering because such physical cues endowed by materials not only have potential to promote the regeneration of the damaged bone tissues, but also can avoid using expensive growth factors or DNA demethylation agents. At the same time, these proven micro-/nanotopographical cues also provide paradigms in guiding the design and construction of specific biomedical devices for the orthopaedic regenerative medicine.

Still, a huge gap exists to translate the topographical cues into clinical practices because (1) current success mainly is limited at two-dimensional (2D) models.[6] For practical clinical applications, however, three-dimensional (3D) stereo-scaffolds generally will be used; (2) most of the used substrates in recent reports for constructing nanotopographis, like PMMA,[1] titanium,[2] and silicon,[4] are either unidentified in clinical practice, or non-degradable and non-similar in chemical components with hard tissues, thus these nanotopographies are not optimal, even unsuitable for implanting into bone defects for hard tissue regeneration.

The calcium phosphate (CaP) relative materials, because of the similarity in chemistry with the inorganic minerals of hard tissues, good biocompatibility and osteoconductivity, always become one of the most considered hard repair materials,[7-10], and now the CaP relative materials have applied widely in the clinical practice.[11,12] Therefore, it can be significant if the CaP relative materials can be processed into 3D scaffolds with osteoinductive micro-/nanotopographies to overcome current limitation.

Currently, the processing of the CaP relative materials into 3D porous ceramics for repairing the damaged bones has been studied well.[12-15] To improve the repairing ability of porous CaP ceramics, the porous CaP ceramics with different porosities possess good bioactivities.[16-18] Still, little attention has been paid to incorporate the micro-/nanotopographical cues into the 3D CaP ceramics.[19,20] Recently, Xia et al have demonstrated that the CaP materials with specific surface nanostructures could mediate the osteogenic differentiation.[19] We have successfully assembled the apatite nanorods into 3D porous CaP ceramics, and the biological experiments have demonstrated that such hierarchally-structured 3D porous ceramics could mediate the osteogenic commitment of MSCs.[20]

Although the CaP materials with specific nanotopographies indicated the abilities of mediating osteogenic differentiation of MSCs, the methods of preparing the CaP nanotopographies were somewhat complex. For example, in our previous work, a hydrothermal process need be employed to grow the apatite nanorods.[20] Such process without doubt added the preparation process and thus increased the cost of manufacture. Alternately, in this work we prepared another kind of apatite nanostructure-constructed, i.e., the apatite nanosheet-constructed porous CaP ceramics. Such structure of the CaP ceramics were prepared by hydrolysing a kind of α-tricalcium phosphate (TCP) contained porous biphasic calcium

[a] National Engineering Research Center for Biomaterials, Sichuan University, Chengdu, 610064, P. R. China. E-mail: hyl@scu.edu.cn
[b] Department of Pharmacy of the First Hospital, Jilin University, Changchun, 130012, P. R. China
† Footnotes relating to the title and/or authors should appear here.

phosphate (BCP) ceramics, and such method demonstrated was simple, repeatable, and cost-effective.

Experimental

Materials

$Ca(NO_3)_2{\cdot}4H_2O$, $(NH_4)_2HPO_4$, HCl, NaOH, H_2O_2, and methylcellulose were analytical reagent (AR) and were purchased from Chengdu Kelong Chemical Reagent Co. The used water was deionized water.

Powder synthesis

Different CaP powders, including hydroxyapatite (HAP), TCP, and BCP powders were synthesized using the co-precipitation method at first.[21] In brief, the $(NH_4)_2HPO_4$ solution was added gradually into a reactor containing the $Ca(NO_3)_2$ solution. The reactor was protected using nitrogen atmosphere. The molar ratio of Ca/P was controlled at 1.5-1.67 for synthesizing different CaP powders. The pH of the solution was maintained at a constant value by adding 30% ammonium hydroxide solution. The synthesis conditions, including pH (7-11), temperature (25-95 °C), Ca/P molar ratio (1.5-1.67) were adjusted in light of the aim products. After the reaction finished, the formed precipitations were filtered without washing and dried at 100 °C.

The dried precipitations then went through a high temperature calcination (at air and the as-prepared samples were heated by 2 °C/min up to 600 °C, and at 600 °C the samples were calcined for 6 h, and then the samples were cooled by 2°C/min to room temperature), and the calcined products subsequently were ground using the jet mill to obtain the ultrathin CaP powders.

Preparation of the AN-PCs

At first the prepared CaP powders (including HAP, BCP, and TCP) were moulded into porous ceramics (cylinders: height: 15 mm; diameter: 10 mm. For cell culture and in vivo implanting, the height of porous ceramics was cut into 1.5 mm) by combing the hydrogen peroxide gas foaming method and high temperature calcination.[22] In brief, an aqueous solution containing 1 wt.% methylcellulose as dispersant and viscous agent and H_2O_2 (the volume ratio of H_2O_2 to the methylcellulose-contained solution is 6 vol.%) as a vesicant were added to the CaP powders to form the CaP slurry. The CaP slurry then was heated by microwave for 30–60 s and the foamed slurry was poured rapidly into the cylindrical moulds with good permeability. After drying at 50-60 °C for 24 h, the as-prepared green porous CaP bodies were sintered at air by heating the green bodies by 2 °C/min up to 1250 °C, and at 1250 °C the temperature was kept for 6 h, and then the sintering temperature decreased by 2°C/min to room temperature to obtain the porous CaP ceramics. The pore sizes of the as-prepared ceramics were assessed using a scanning electron microscopy (SEM).

The as-sintered porous ceramics with different chemical components (HAP, BCP, and TCP) then were soaked in the deionized water for 24 h. Finally the soaked porous ceramics were dried in air. In a control experiment, the as-sintered porous ceramics were put into a thermostatic water bath with adjustable humidity for 24 h to understand the effect of water on the growth of the apatite nanosheet.

To detect the apatite nanosheet growth over time, the porous ceramics soaked in water were transferred into acetone at once at the designed time points (1 and 24 h) to impede the growth of apatite nanosheets.

To understand the effect of pH to grow the apatite nanosheets, the pH of the soaked water solution (pH: 8 and 11) was adjusted using HCl and NaOH.

Characterization

The morphologies of all samples were observed using the SEM (Hitachi S-4800) and a transmission electron microscopy (TEM, Tecnai G2 F20 S-TWIN). For SEM test, the samples were treated by gold sputter coating for 30 s. For TEM test, the apatite nanosheets were scraped off from the surface of the porous ceramics and the separated powders were loaded on the carbon film-coated copper grid. Then a drop of ethanol was dropped on the copper grid. After ethanol evaporated, the loaded powers were fixed on the copper grid. The phase compositions of the samples were analysed by an X-ray diffraction (XRD, XD1000, Cu Kα radiation, λ = 1.5406 Å) at a scanning rate of 0.02°/s in 2ϑ ranging from 20 to 50°. To XRD analysis, the samples were ground into powders, and the phasic component of the CaP ceramics was decided In light of the peak intensity ratio of $I_{\alpha\text{-TCP }(170)}/(I_{HAP(211)}+I_{\alpha\text{-TCP }(170)})$.[23] A Fourier transform infrared spectroscopy (FTIR, PerkinElmer Autoimage) was employed to analyze the chemistry of the ground samples. A mercury intrusion porosimetry (MIP, micromeritics Auto Pore IV9500) was used to measure the pore size and porosity of samples. Hg intrusion and extrusion experiments were performed over a pressure range of from 0.1 up to 60000 psi. The pore size range assessed ranged from 1000 um down to ~100 nm.

Cell culture

Bone marrow MSCs were harvested from thigh-bones of neonatal rabbits. The harvested MSCs were passaged and the passage 3 MSCs were used to seed into samples. The culture medium was a mixed system of α-MEM (89 vol.%), fetal bovine serum (10 vol.%, FBS; Gibco, USA), and penicillin–streptomycin (1 vol.%, PS; Gibco, USA). After sterilization, the samples were placed in the 24-well plates (Corning, USA) and seeded with 2×10^4 cells/well in 2 mL of medium. Then the cell-seeded samples were cultured at 37 °C in a humid, 5 % CO_2-contained atmosphere. The culture media were changed at intervals of 3 days and the samples were removed at defined time point (from 1 day to 21 days) for biological analyses.

SEM of cells

Adherent cells on samples were fixed with 2.5% glutaraldehyde for 4 h. After washing with Mili-Q water, the cells were dehydrated in a graded ethanol series from water through 10%, 20%, 50%, 75%, 80%, and 95% ethanol with time

interval 15 min, and last through 100% ethanol for 30 min. The samples then were placed in a critical point drying apparatus (Hitachi), where ethanol was replaced with liquid CO_2, which was heated to 27 °C and changed state to its gaseous phase. The CO_2 gas was vented and then samples coated with gold using sputter coater. The samples were tested using SEM.

Live-dead analyses

The MSCs cultured in different ceramics over time were observed by a confocal laser scanning microscopy (CLSM, Olympus IX 95). Before observation, the cell-adhered ceramics were rinsed by sterile phosphate buffered saline (PBS) and stained by fluoresein diacetate (FDA) for live cells and propidium iodide (PI) for dead cells.

Phalloidin staining

The cultured cells (3 days) were rinsed two times using PBS briefly to remove media components, and then cells were fixed in 3.7% formaldehyde in PBS (freshly prepared) for 5 min at room temperature and washed 3 times in PBS. Cells were dehydrated with acetone, permeabilized with 0.1% Triton X-100 in PBS, and washed again in PBS. Cells were stained with a 50 mg/ml rhodamine-phalloidin conjugate (Sigma, Catalog Number P1951) solution in PBS (containing 1% DMSO from the original stock solution) for 40 minutes at room temperature. The samples were washed 3 times with PBS to remove unbound phalloidin conjugate and the nuclei were stained with DAPI at 37 °C.

Alkaline phosphatase staining

Cells were stained for alkaline phosphatase (ALP) using Sigma kit number 86C according to the manufacturer's instructions. In brief, the cells adhered on the samples were fixed and stained using the ALP staining solutions, and stained ALP was scored in light of the table of the characteristics of ALP scoring shown in the manufacturer's instructions.

Osteogenesis-related gene expression

The expressions of osteogenesis-related genes were evaluated by quantitative real-time polymerase chain reaction (QRT-PCR). The cells cultured on samples for 4, 7, and 14 days were rinsed twice with PBS and their total RNA was isolated using the Trizol reagent (Invitrogen, Carlsbad, CA) according to the manufacturer's protocol and collected by ethanol precipitation. 1 μg RNA from each sample was reversed transcribed into complementary DNA (cDNA) using an iScript cDNA Synthesis Kit (Bio-Rad, CA). Equal volumes of cDNA were used to program QRT-PCR reactions specific for some osteogenesis-related mRNAs encoding, including core-binding factor alpha-1 (Cbfa1), bone morphogenetic protein-2 (BMP-2), collagen-I (COL-I), and osteocalcin (OCN). Reactions were performed using PCR Tube Strips (TCS0803) (Bio-Rad, CA) and thermocycling in a CFX96 real time thermocycler (Bio-Rad, CA). Relative mRNA abundance was determined by the 2-ΔΔCt method and reported as fold induction. GAPDH abundance was used for normalization. The obtained results then were normalized by the live cell numbers.

In vivo ectopic implant

The in vivo procedures were undertaken strictly in accordance with state regulations and laws and in accordance with the Standing Committee on Ethics in China (State Scientific and Technological Commission of China).[24] The animal experiments were approved by Jilin University Committee on Animal Care and were conducted at Center of Laboratory Animal Science, School of Basic Medical Sciences, Jilin University. All experiments involving animals were performed in accordance with the approved guidelines.

3 Adult male New Zealand rabbits with weight 2.5-3 kg were used in this study. The rabbits were anesthetized by intravenous injection of 2 mg/kg pentobarbital sodium. The operations were performed under sterile conditions. Then the subcutaneous implantation was carried out, i.e., the ceramics were implanted into back muscles of rabbits. In a rabbit, 4 pieces of porous ceramics were implanted. After the implantation was finished, the fascia and subcutaneous layers were closed with silk sutures and the skin was closed with surgical skin staples. To harvest the specimens, the rabbits were sacrificed after 2 month-operations with overdose of pentobarbital sodium, and the intramuscular implants were retrieved.

Histological examinations

The intramuscular implants were fixed in 10% buffered formalin for 48 h, decalcified in 10% EDTA (pH 7.0) for 20 d, and embedded in paraffin. The embedded specimens then were sectioned using a high-speed precision microtome (LEICA SP1600, Germany). Finally, the sections of the ground specimens were stained with toluidine blue (TB) for optical microscopy observation.

Statistical analysis

All data were presented as means ± standard deviations (s.d.). To test the signification of observed differences between the study groups, an unpaired Student t-test was applied. A value of $p < 0.05$ was considered to be statistically significant.

Results

The preparation of the AN-PCs

Fig. 1(a-b) show that the as-prepared porous ceramics have abundant macropores, and the average pore size of these macropores is 450 μm. The magnified image (Fig. 1b1) shows the porous BCP ceramics are composed of grains. The XRD pattern (Fig. 2a) demonstrated that the as-prepared porous ceramics were biphasic, consisting of α-TCP (JCPDS: 09-0348) and HAP (JCPDS: 46-0905). In light of the peak intensity ratio of α-TCP and HAP, the α-TCP phase in biphasic ceramics is 0. 4323.

After the as-prepared porous BCP ceramics were soaked in deionized water for 24 h, the nanosheets were grown at the wall surfaces of the BCP ceramics, as shown in Fig. 1(c-c11). These nanosheets showed large diameter (~3-7 μm), but very

thin thickness (~30 nm, see the TEM images shown in Fig. 1d). The XRD pattern (Fig. 2a) indicated that the soaked ceramics were transferred into HAP phase completely, suggesting that both the substrates and the formed nanosheets were composed of the HAP phase. The FTIR patterns (Fig. 2b) showed that besides the OH groups (νOH, 3573 cm^{-1}, δOH, 631 cm^{-1}) and the PO_4 groups (ν_1PO_4, 958 cm^{-1}, ν_3PO_4, broad band 1020–1120 cm^{-1}, and ν_4PO_4, 569 cm^{-1} and 601 cm^{-1}),[25] , a new adsorption peak at 873 cm^{-1}, which can be attributed to the P-O-H vibration in the HPO_4^{2-} groups,[25,26] emerged in the soaked ceramics. The FTIR results suggested that the formed nanosheets are composed of the Ca-defected HAP.[27] The MIP analysis indicates that the open porosity of the primary BCP ceramics is 52.30 ± 0.95 % and two pore size distributions are presented: 0.2-90 μm and 100-350 μm (Fig. 2C). Although the apatite nanosheets were grown, pore size hardly had changed. Nevertheless, the open porosity dropped slightly down to 49.4± 0.84 %. The decrease of open porosity, as can be seen from Fig. 2(c), could be attributed to the decrease of small pores (0.2-90 μm). It suggested that during the apatite nanosheets growth, some small pores were blocked up or filled.

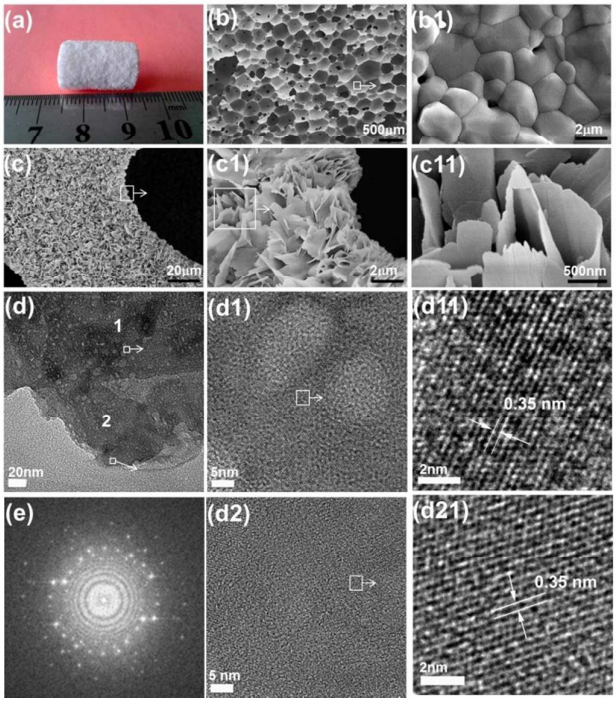

Fig. 1. (a) Photography and (b, b1) SEM images of the as-prepared porous BCP ceramics (b1 is the local magnification of b); (c, c1, & c11) SEM images of apatite nanosheets on the wall surfaces of porous ceramics after the BCP ceramics had been soaked for 24 h (c1 is local magnification of c and c11 is the local magnification of c1). (d, d1, d12, d2 &d21) TEM images of the as-grown apatite nanosheets. In these images, (d1) and (d2) are the middle magnification of the local 1 and local 2 in (d), and (d11) and (d21) are the local high-magnification TEM images from (d1) and (d2). (e) The FFT pattern of the as-grown apatite nanosheets.

The ultrastructure of the formed apatite nanosheets was further investigated using a TEM and the corresponding results are shown in Fig. 1(d-e). The low-magnification of TEM image (Fig. 1d) showed that some nanopits distributed in the nanosheets. The middle-magnification of TEM image (Fig. 1d1) showed the diameter of the nanopits is about 10-20 nm. The FFT pattern and middle-magnification of TEM images (Fig. 1d-e) showed that the nanosheets are multi-crystalline. The highly-magnified TEM images (Fig. 1d1i and 1d2i) showed that although the crystallographic direction of two selected area was different from each other, they shared same lattice spacing, 0.35 nm, which could be corresponded to the $d_{(002)}$ of the HAP crystals.[28] Based on above analyses, the as-grown apatite nanosheets are composed of multi-crystalline, HAP crystal phase, and the main chemical component is HAP with trace of HPO_4.

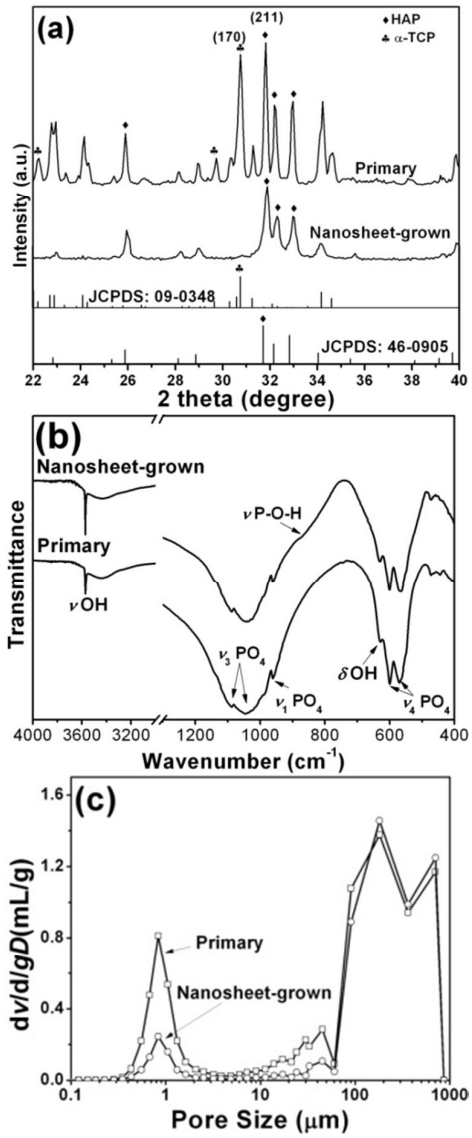

Fig. 2. (a) XRD, (b) FTIR, and (c) MIP of the primary and apatite nanosheet-constructed porous BCP ceramics.

Experiments demonstrated that the porous BCP ceramics were sensitive to water. When these ceramics were kept at the

humid condition for 24 h (25 °C, 65 %RH), the grain surfaces would hydrolyse slightly to form some small dots (Fig. 3a), and when these ceramics were soaked into water for 1 h, small sheet-like structures grew from the grain surfaces (Fig. 3b-b1). The nanosheets continuously grew with immersion time, and experiment showed that after 24 h immersion, the growth of nanosheets caused and larger apatite nanosheets formed (The size and shape of the as-grown nanosheets did not change with longer time of immersion) (Fig. 3c).

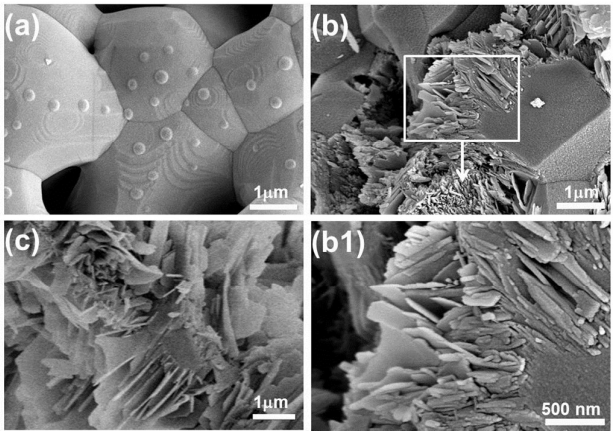

Fig. 3. The growth of apatite nanosheets in the porous BCP ceramics in humid air for 24 h (25 °C, 65 %RH) (a), and in deionized water for 1 h (b, b1) and 24 h (c).

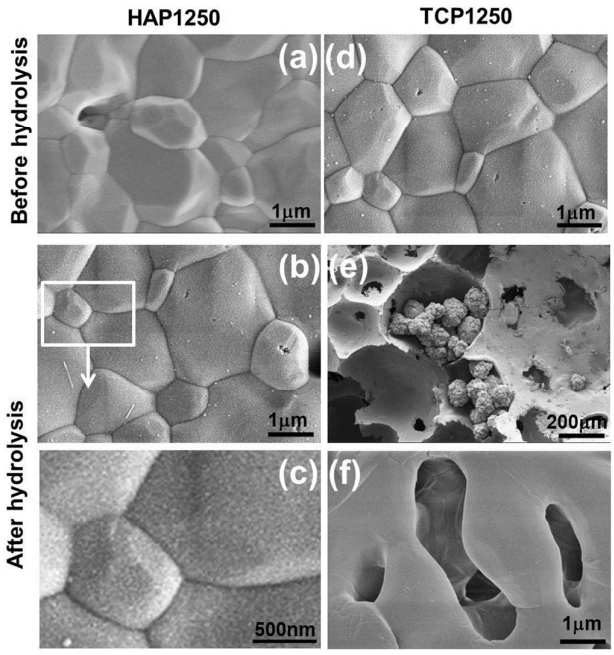

Fig. 4. SEM images of the pure HAP and α-TCP ceramics (both were sintered at 1250 °C for 6 h) before and after water immersion. (a) The pure HAP ceramic. (b) and (c) are low and high magnified images of the water-soaked HAP ceramic. (d) The pure α-TCP ceramic. (e) and (f) are the low and high magnified images of the water-soaked α-TCP ceramic, respectively.

Experiments showed that the chemical components also affected the growth of the apatite nanosheets. In an control experiment, the pure HAP and α-TCP porous ceramics (Figure 4a and 4d) were prepared (both have been calcined at 1250 °C for 6h) and soaked in water for 24 h. Fig. 4(b,c) showed that the grain surfaces of the HAP ceramics hardly have changed. In contrast, Fig. 4(e,f) showed that the gain surfaces of α-TCP ceramics were eroded and some small pores formed at microscale, and some large grain aggregates with diameters 5-200 um were deposited in ceramic porosities. Obviously, it can be attributed to the part hydrolysis of α-TCP from the grains and the hydrolysed components released into water and recrystallize into the large CaP grain aggregates.

Furthermore, the effect of pH to the apatite nanosheet growth also investigated. Fig. 5 shows that when the PH ≥ 7, the increase of reactive pH hardly affected the structure of the as-grown apatite nanosheets. Nevertheless, the FFT pattern and TEM images demonstrated that the apatite nanosheets grown in higher pH solution presented higher crystallinity. As shown in Fig. 5(b), the apatite nanosheets grown in a solution with pH 11 almost indicated a single apatite crystal structure. It demonstrated that the growth of the apatite nanosheets at high pH environment can improve the crystallization of the apatite nanosheets.

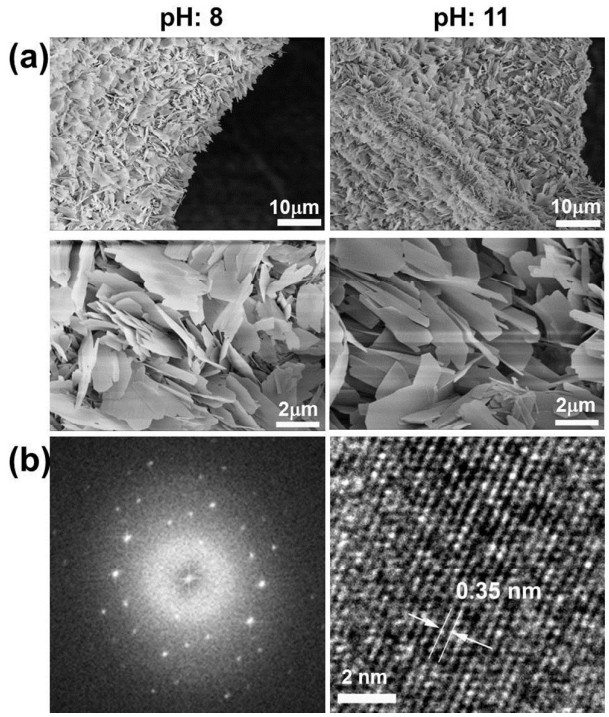

Fig. 5. The effect of pH on the apatite nanosheet growth. (a) SEM images of apatite nanosheets grown in pH 8 and 11 solutions. (b) FFT (left) and RT-TEM (right) images of the apatite nanosheets grown in a solution with pH 11.

Cytocompatibility

The biological effects of the as-prepared AN-PCs then were investigated. For comparison, the HAP grain-constructed porous ceramics were prepared as a control. At first we tested the cytocompatibility of the AN-PCs using MSCs. Although it is well known that HAP is a kind of biomaterials with excellent biocompatibility because of its chemical similarity with mineral

components of hard tissue, the HAP ceramics with specific morphology possibly affects the survival of cells.[20] Fig. 6 shows that the number of live and dead MSCs in the AN-PCs was always similar with that in the HAP grain-constructed porous ceramics. It showed that the apatite with the nanosheet-like structure did not cause cytotoxicity. Nevertheless, the proliferation prolife of the MSCs in the AN-PCs was not always accordant with that in the HAP grain-constructed ceramics. As shown in Fig. 6, the MSCs in the AN-PCs presented lower cell number at day 5. A possible explanation is that the differentiation of the MSCs in the AN-PCs towards the osteogenic lineage occurred at day 5.

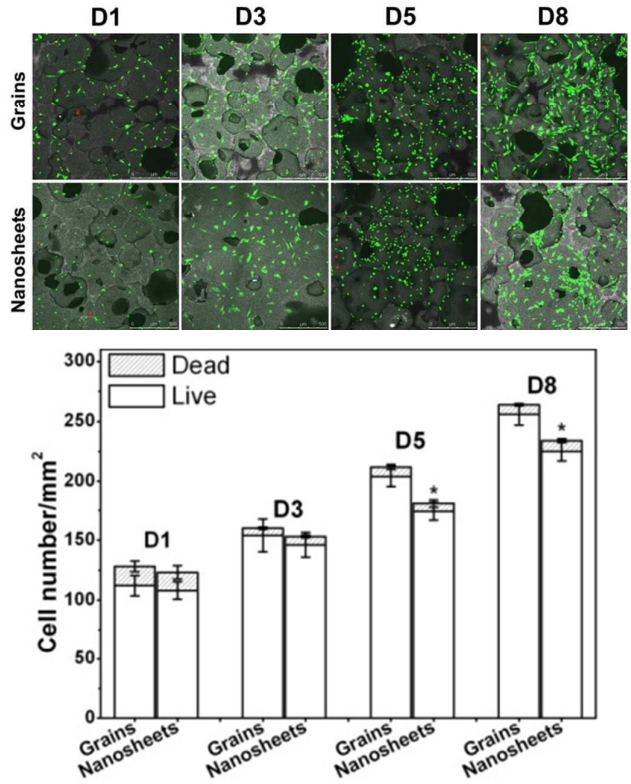

Fig. 6. Dead-live staining and cell proliferation in the apatite grain-constructed and the apatite nanosheet-constructed ceramics (mean ± S.D., n = 3, * p< 0.05* when compared with the live cells in the HAP grain-constructed ceramics).

Cell spreading

Then the spreading of the MSCs in the AN-PCs was investigated, and the corresponding results are shown in Fig. 7. The low-magnification SEM image (Fig. 7a) shows that the cells well spread on the surface of nanosheets, and the high-magnification SEM image (Fig. 7a1) showed that the cellular filopodia were fond of anchoring on the surface of nanosheets. Also, the cells also can spread well on the HAP grain-constructed ceramics (Fig. 7b-b1). Still, the area of cell spreading on the HAP grain-constructed ceramics is significant smaller than that on the AN-PCs (Fig. 7c). It shows that the apatite nanosheets-constructed surfaces promote the cell spreading. Phalloidin staining further demonstrated that above results. As shown in Fig. 7(a2,b2), MSCs assembled the stress fibers on both sample surfaces. Also, the number of the stress fibers assembled by the MSCs on the nanosheets-constructed surfaces was significant higher than that on the surfaces of the HAP grain-constructed ceramics (Fig. 7d). Taken together, above results showed that the apatite nanosheet-constructed surfaces promoted cell adhesion and spreading, and the MSCs adhered on such surfaces could produce lager cytoskeleton tension than on the HAP grain-constructed surfaces.

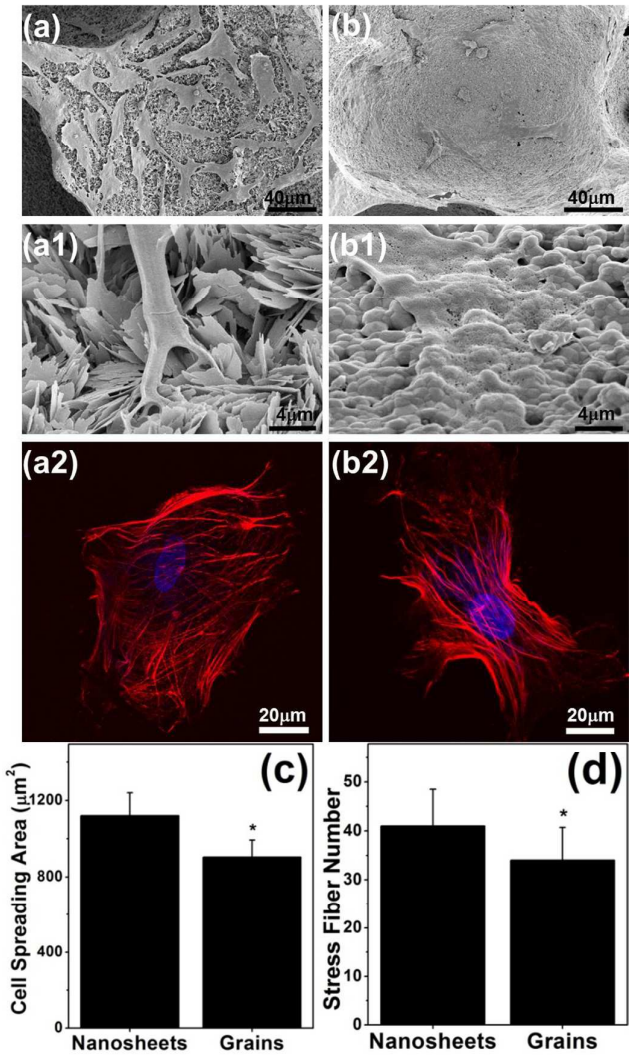

Fig. 7. The adhesion and spreading of the MSCs cultured in the AN-PCs (a-a1, SEM images, a2, phalloidin staining image) and in the HAP-grain-constructed ceramics for 3 days (b-b1, SEM images, b2, phalloidin staining image). (c) Cell spreading area and (d) stress fiber number of the MSCs adhered in both samples (mean ± s.d., n=3, * p < 0.05).

Osteogenic commitment of MSCs

To detect the osteogenic commitment of MSCs, alkaline phosphatase (ALP) activity of the MSCs cultured in the AN-PCs was monitored over time. ALP is used because ALP is a potent and significant predictor of osteogenic lineage commitment, and also is a highly specific marker and inducer of bone formation.[29-31] Fig. 8(a) showed that the expression of ALP

began from day 7, and at day 10, abundant ALP could be observed within the AN-PCs. By contrast, the MSCs in the HAP grain-constructed ceramics always did not secret ALP within 10 days (Fig. 8a).

In addition to ALP, Fig. 8(b) shows that at day 21, the MSCs cultured in the AN-PCs expressed abundant mineral nodules, but not in the HAP grain-constructed ceramics. The formation of mineral nodules in the AN-PCs further verified that the osteogenic differentiation of MSCs was mediated by the apatite nanosheet-constructed topographies.

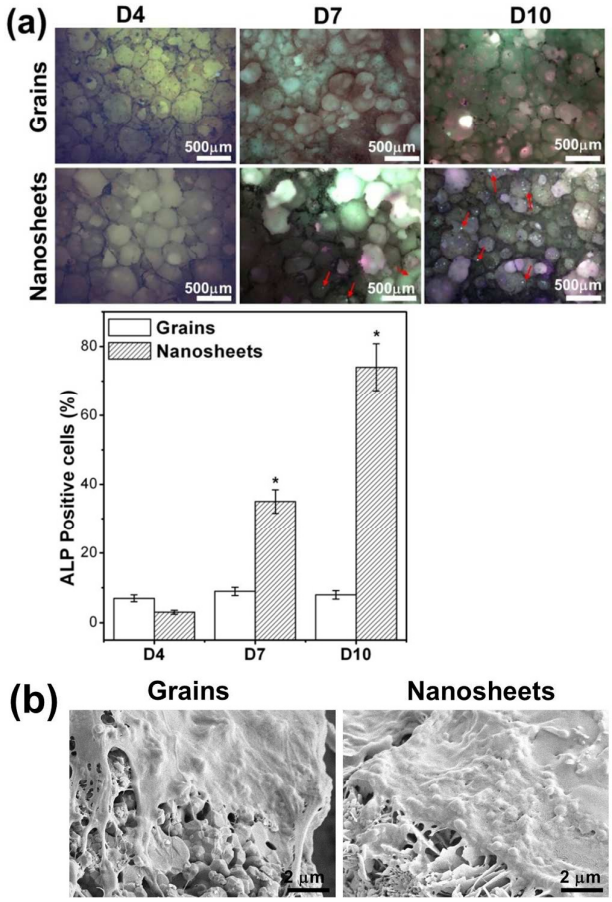

Fig. 8. (a) ALP staining (the red arrows denote the ALP) and (b) SEM images (21 days) of the MSCs cultured in the HAP grain-constructed and the apatite nanosheet-constructed porous ceramics (mean ± s.d., n = 3, * $p < 0.05$).

To further understand whether the osteogenesis of the MSCs in the AN-PCs abides by the classical osteogenic timelines, a quantitative (q-RT) PCR was used with primers to detect whether some important osteoblast-relative genes, including Cbfa1, BMP-2, Col-I, and OCN, are activated in the correct order to permit differentiation, and the resulting expression was shown in Fig. 9. The transcriptional activator Cbfa1 (core-binding factor-1, also known as osteoblast specific *cis*-acting element-2 [Osf2]), is expressed in preosteogenic condensations but then strictly in the osteogenic cell lineage.[31] Fig. 9 showed that the expression of Cbfa1 by the MSCs started at day 7 and the cells expressed highest level of Cbfa1 at day 14, and the expression level dropped at day 21. BMP-2, known to be expressed in condensation in vivo and in osteogenic differentiation, was expressed at day 7, and its expression level increased gradually and reached maximum value at day 14. Then the expression was downregulated. Different from Cbfa1 and BMP-2, the expression of Col-I by the cells cultured in both samples increased continuously, and the expressed level of Col-I in the AN-PCs is similar with that in the HAP grain-constructed ceramics. In addition, Figure 9(c) shows that the Col-I expression quantity by cells is higher than Cbfa1 and BMP-2. Such result suggested that the matrix has small influence on the expression of Col-I. A kind of important mineral-relative gene, OCN, which only can be expressed by osteoblasts, and is involved in the sequestration of Ca^{2+} for mineralization,[33] was expressed highly in the AN-PCs. The high expression of OCN can be concluded as the formation of the bone-like mineral nodules, as demonstrated in Fig. 8(b). The temporal analysis of osteogenic phenotypical expression shown above confirmed the osteogenic differentiation of MSCs in the AN-PCs is similar as classical osteogenic timelines.[34]

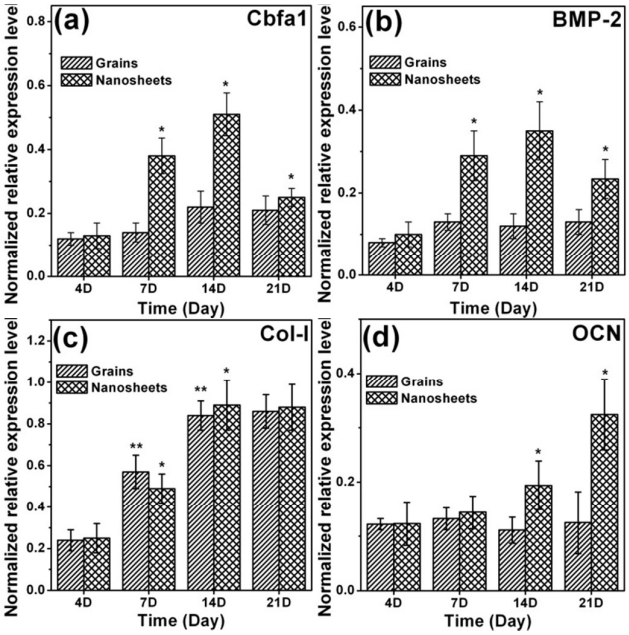

Fig. 9. qRT-PCR results of cells cultured in the apatite nanosheet-constructed and the HAP grain-constructed porous ceramics over time (mean ± s.d., n = 3, * and ** $p < 0.05$ when compared with the previous datum).

Taken together, these evidences, *i.e.*, high expression of osteogenic proteins and genes, as well as the formation of mineral nodules, well verified the osteogenic differentiation of MSCs mediated by the apatite nanosheet-constructed topographies. The MSCs cultured in the AN-PCs could be induced into osteoblasts. In contrast, the HAP grain-constructed ceramics did not mediate osteogenic differentiation of MSCs within such culture period.

Histological examination

Finally, the as-prepared samples were implanted in the back muscles of rabbits for 60 days. The purpose of ectopically-implanting the samples into back muscles of rabbits can test the osteoinductivity of samples.[35,36] Fig. 10(a) showed that the newly formed bone inside the pores of the AN-PCs could be observed clearly. Especially, the newly-formed bone in some pores (the arrow in Figure 10a) grew towards the structure of the Haversian system. In contrast, only connective tissues grew into the porosities of the HAP grain-constructed ceramics (Fig. 10b). The ectopical bone formation within the pores of AN-PCs showed that the AN-PCs possessed of the biological function of osteoinductivity.

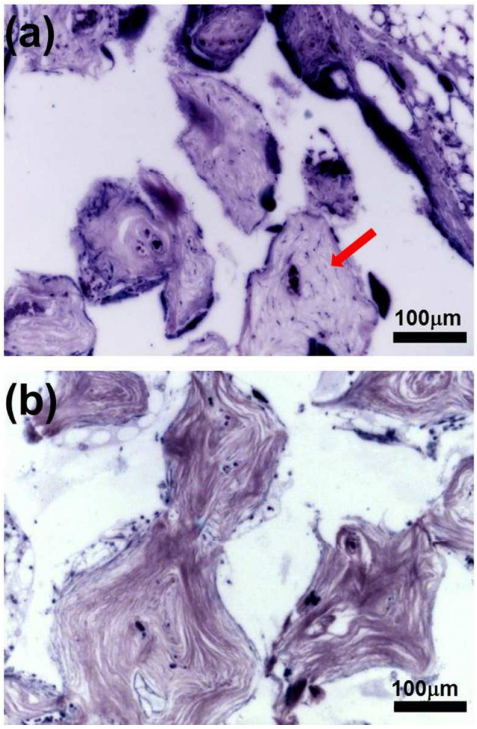

Fig. 10. TB-stained histological sections of (a) the apatite nanosheet-constructed and (b) the HAP grain-constructed ceramics implanted into the rabbit's back muscles for 60 days.

Discussion

The growth of apatite nanosheets in porous BCP ceramics

Apatite nanosheets are one of important nanostructural units of the CaP materials. The controllable assembly of the apatite nanosheets into the specific architectures possibly enhances the performance of the biomaterials. In a conventional method, a simple immersion of the biomaterials in a simulated body fluid (SBF) could grow the apatite nanosheets on their surfaces.[37] However, such method presents two shortcomings. The first is that the condition of growing the apatite nanosheets is harsh. e.g., it requires that the used soaked vessels are smooth and do not initiate the crystallization of apatite. The other is that the reproducibility cannot be ensured completely. Alternately, herein we demonstrated that the apatite nanosheets could be easily assembled into porous CaP ceramics to form the AN-PCs by hydrolysing the α-TCP-contained BCP ceramics (Fig. 1-3). Our experiments have shown that the growth condition of the apatite nanosheets is moderate and the growth process can be reproduced completely.

In our experiment system, the α-TCP components shown played key role in driving the growth of the apatite nanosheets because experiments have demonstrated no apatite nanosheets could grow when the pure HAP ceramics were soaked (Fig. 4). It has well known that α-TCP could hydrate to a calcium-deficient hydroxyapatite in aqueous solution and grow into different morphologies.[38] Therefore, in our BCP ceramics, when the BCP ceramics met water the α-TCP components surely initiate the hydrolysis and recrystallization on the surfaces of the BCP ceramics.

Besides α-TCP, the HAP phase in the substrate ceramics also played important role in mediating the formation of the apatite nanosheet structures. Experiments demonstrated that when the pure α-TCP ceramics were soaked, only the separated apatite particles were formed (Fig. 4). It has well known that the epitaxial growth of crystals on a substrate was decided by the crystal structure of the substrate.[37,40] No apatite nanosheets could grow in the pure α-TCP ceramics because the recrystallized calcium-deficient hydroxyapatite phase could not match the α-TCP crystal phase of substrate ceramics. In contrast, in the HAP-contained ceramics, the HAP phase allowed the epitaxial growth of the calcium-deficient hydroxyapatite phase on their surfaces.[41,42]

In general, under the alkaline condition, the increase of pH is favourable for the growth of the HAP phase.[43] Also, our experiments showed that at the same time of keeping sheet structure, the increase of pH enhanced the crystallization of apatite nanosheets. It suggested that the high pH of the soaked solution is helpful for the apatite nanosheet growth.

Biological effects of the AN-PCs

As mentioned above, the accumulating evidences have demonstrated that the specific topographical cues could mediate osteogenic commitment of MSCs. Still, these evidences mainly came from the two-dimensional models. A few data have shown that the specific topographical cues in three-dimensional models also could work.[19,20] For the practice application, however, the topographical cues should be constructed into three-dimensional scaffolds. Therefore, in our work, the assembly of the apatite nanosheets into three-dimensional porous ceramics significantly shortened the gap of from the concept of mechanotransduction, *i.e.*, extracellular physical forces sponsored from materials features can be converted into chemical signals to alter the fate decision of MSCs, to the clinical applications.

The underlying biological mechanism of the topographical cues mediating the osteogenic commitment of MSCs is these cues could mediate MSCs to form a strong cytoskeletal tension,[44] which could promote cells to organize the stress fibers to propagate the stress to nucleus.[45] Also, our experiments demonstrated that the apatite nanosheets-constructed

surfaces induced MSCs to produce a very high cytoskeletal force, which triggered subsequent osteogenic commitment of MSCs. In contrast, The MSCs adhered on the HAP grain-constructed surfaces believed could not promote the organized cytoskeletal filaments to produce a high-enough tensed cytoskeletal force, thus the mechanical stress exerted to the cytoskeletal filaments decayed rapidly over a short distance in space, thereby the stress could not be propagated to nucleus. Therefore, the osteogenic differentiation of MSCs did not occur in the HAP grain-constructed ceramics.

In addition, our in vitro and in vivo experiments showed that although the topographical cues were assembled into three-dimensional space, they share the same biological mechanism of mediating the osteogenic commitment of MSCs. It shows that the osteogenic differentiation of MSCs mediated by the topographical cues was available not only on 2D substrates, but also in 3D structures. In fact, as can been seen from Fig. 7, our macropores have so large diameter as to render the curvature of macropores small with respect to a single cell, and the individual cells spread on the substrates of pore wall are quite flat. Therefore, the curvature of macropores postulated has little effect on mediating the commitment of MSCs.

Furthermore, although many topographical cues have been demonstrated to have the ability of mediating the osteogenic commitment of MSCs, these evidences mainly be limited at in vitro results. Herein, besides the in vitro experiments, the experiments of in vivo implant also were performed, and the results showed that after the AN-PCs were implanted into body of animals ectopically, the new bones could form within the pores of the AN-PCs. Such results suggested that the topographical cues could work at in vivo environment, too.

It needs to clarify that the new bone could form heterotopicaly in the AN-PCs because immature cells, including MSCs, have been recruited into the AN-PCs.[46-48] Thus we can speculate in light of the in vitro and in vivo results that the recruited MSCs would be stimulated by the AN-PCs to develop into osteoblasts. Still, a large number of experiments need be performed to clarify the recruited cells.

Conclusion

In summary, we have successfully fabricated the AN-PCs by foam moulding, high heat sintering and then water soaking the α-TCP/HAP-contained porous BCP ceramics. Experiments demonstrated that the growth of the apatite nanosheets in the ceramics mainly was controlled by the α-TCP components and the HAP components. Our biological experiments showed that the AN-PCs had excellent cytocompatibility, and alone could regulate MSCs to differentiate into osteogenic lineages, and the in vivo ectopic-implant showed that the AN-PCs could induce the formation of new bones. Especially, because the fabrication of such 3D nanotopographies is simple, repeatable, and low-cost, and the tailored materials, calcium phosphates, do not contain the elements that human body does not have, and now have been widely used in clinical practice, the AN-PCs reported here depict a good prospect for a range of applications in regenerative medicine of hard tissues.

Acknowledgements

This work was supported by the National Natural Science Foundation of China (Grant 31570977).

Notes and references

1 M. J. Dalby, N. Gadegaard, R. Tare, A. Andar, M. O. Riehle, P. Herzyk, C. D. W. Wilkinson and R. O. C. Oreffo, *Nature Mater.*, 2007, **6**, 997-1003.
2 T. Sjöström, M. J. Dalby, A. Hart, R. Tare, R. O.C. Oreffo and B. Su, *Acta Biomater.*, 2009, **5**, 1433-1441.
3 S. Oh, K. S. Brammer, Y. S. J. Li, D. Teng, A. J. Engler, S. Chien and S. Jin, *Proc. Natl. Acad. Sci. USA*, 2009, **106**, 2130-2135.
4 S. W. Kuo, H. I. Lin, J. H. C. Ho, Y. R. V. Shih, H. F. Chen, T. J. Yen and O. K. Lee, *Biomaterials*, 2012, **33**, 5013-5022.
5 O. Chaudhuri and D. J. Mooney, *Nat. Mater.*, 2012, **11**, 568-569.
6 A. M. Ross, Z. Jiang, M. Bastmeyer and J. Lahann, *Small*, 2012, **8**, 336-355.
7 H. Yuan, H. Fernandes, P. Habibovic, J. de Boer, A. M. C. Barradas, A. de Ruiter, W. R. Walsh, C. A. van Blitterswijk and J. D. de Bruijn, *Proc. Natl Acad. Sci. USA*, 2010, **107**, 13614-13619.
8 S. Oh, N. Oh, M. Appleford and J. L. Ong, *Am. J. Biochem. Biotechnol.*, 2006, **2**, 49-56.
9 C. Zhou, Y. Hong and X. Zhang, *Biomater. Sci.*, 2013, **1**, 1012-1028.
10 K. Wang, C. Zhou, Y. Hong and X. Zhang, *Interface Focus*, 2012, **2**, 259-277.
11 L. L. Hench, *J. Am. Ceram. Soc.*, 1998, **81**, 1705-1728.
12 Y. Hong, H. Fan, B. Li, B. Guo and X. Zhang, *Mater. Sci. Engineer. R*, 2010, **70**, 225-242.
13 Y. Huang, X. Jin, X. Zhang, H. Sun, J. Tu, T. Tang, J. Chang and K. Dai, *Biomaterials*, 2009, **30**, 5041-5048.
14 C. Zhang, J. Wang, H. Feng, B. Lu, Z. Song and X. Zhang, *J. Biomed. Mater. Res.*, 2001, **54**, 407-411.
15 W. Habraken, P. Habibovic, M.s Epple and M. Bohner, *Mater. Today*, 2015, **19**, 2, 69-87.
16 H. Yuan, K. Kurashina, J. D. de Bruijn, Y. Li, K. de Groot and X. Zhang, *Biomaterials*, 1999, **20**, 1799-1806.
17 C. Zhang, J. Wang and X. Zhang, *J. Biomed. Mater. Res.*, 2000, **52**, 354-359.
18 U. Ftipamonti, *Biomaterials*, 1996, **17**, 31-35.
19 L. Xia, K. Lin, X. Jiang, B. Fang, Y. Xu, J. Liu, D. Zeng, M. Zhang, X. Zhang, J. Chang and Z. Zhang, *Biomaterials*, 2014, **35**, 8514-8527.
20 Y. Chen, Z. Sun, Y. Li and Y. Hong, *ACS Appl. Mater. Interfaces*, 2014, **6**, 21886-21893.
21 V. M. Rusu, C. H. Ng, M. Wilke, B. Tiersch, P. Fratzl and M. G. Peter, *Biomaterials*, 2005, **26**, 5414-5426.
22 N. O. Engin and A. C. Tas, *J. Eur. Ceram. Soc.*, 1999, **19**, 2569-2572.
23 S. Raynaud, E. Champion, D. Bernache-Assollant and J.- P. Laval, *J. Am. Ceram. Soc.*, 2001, **82**, 359-366.
24 A. W. Peterson, D. J. Caldwell, A. Y. Rioja, R. R. Rao, A. J. Putnam and J. P. Stegemann, *Biomater. Sci.*, 2014, **2**, 1497–1508
25 I. Cacciotti and A. Bianco, *Ceram. Intern.*, 2011, **37**, 127–137.
26 I. V. Fadeev, L.I. Shvorneva, S.M. Barinov and V.P. Orlovskii, *Inorg. Mater.*, 2003, **39**, 947–950.
27 H. C. Park, D. J. Baek, Y. M. Park and S. Y. Yoon, *J. Mater. Sci.*, 2004, **39**, 2531-2534.

28 Z. Zhuang, T. J. Fujimi, M. Nakamura, T. Konishi, H. Yoshimura and M. Aizawa, *Acta Biomater.*, 2013, **9**, 6732–6740.
29 B. K. Hall, *Biol. Rev.*, 1970, **45**, 455-484.
30 T. J. Thompson, P. D. A. Owens and D. J. Wilson, *J. Anat.*, 1989, **166**, 55-65.
31 J. Zernik, K. Twarog and W. B. Upholt, *Differentiation*, 1990, **44**, 207-215.
32 P. Ducy, T. Schinke and G. Karsenty, *Science*, 2000, **289**, 1501-1504.
33 P. Ducy, C. Desbois, B. Boyce, G. Pinero, B. Story, C. Dunstan, C. E. Smith, J. Bonadio, S. Goldstein, C. Gundberg, A. Bradley and G. Karsenty, *Nature*, 1996, **382**, 448-452.
34 G. S. Stein and J. B. Lian, *Endocr. Rev.*, 1993, **14**, 424-442.
35 H. Yuan, H. Fernandes, P. Habibovic, J. de Boer, A. M. C. Barradas, A. de Ruiter, W. R. Walsh, C. A. van Blitterswijk and J. D. de Bruijn, *Proc. Natl. Acad. Sci. U S A.*, 2010, **107**, 13614-13619.
36 T. Albrektsson and C. Johansson, *Eur. Spine J.*, 2001, **10**, S96-S101.
37 F. Lindberg, J. Heinrichs, F. Ericson, P. Thomsen and H. Engqvist, *Biomaterials*, 2008, **29**, 3317-3323.
38 T. Goto, I. Y. Kim, K. Kikuta and C. Ohtsuki, *Ceramics International*, 2012, **38**, 1003-1010.
39 A. Goswami, *Nature*, 1961, **191**, 160-161.
40 I. Boney, *Acta Cryst.*, 1972, **A28**, 508-512.
41 Y. -M. Kong, H. -E. Kim and H. -W. Kim, *J. Biomed. Mater. Res. B: Appl. Biomater.*, 2008, **84B**, 334-339.
42 X. Liu, K. Lin and J. Chang, *CrystEngComm*, 2011, **13**, 1959-1965.
43 K. Furuichi, Y. Oaki and H. Imai, *Chem. Mater.*, 2006, **18**, 229-234
44 R. McBeath, D. M. Pirone, C. M. Nelson, K. Bhadriraju and C. S. Chen, *Dev. Cell*, 2004, **6**, 483-495.
45 N. Wang, J. D. Tytell and D. E. Ingber, *Nature Rev. Mol. Cell Biol.*, 2009, **10**, 75-82.
46 T. Albrektsson and C. Johansson, *Eur. Spine J.*, 2001, **10**, S96-S101.
47 H. M. Frost, *Clin. Orthop. Rel. Res.*, 1989, **248**, 283–293.
48 H. M. Frost, *Clin. Orthop. Rel. Res.*, 1989, **248**, 294-309.

Preparation and biological effects of apatite nanosheet-constructed porous ceramics

Ying Chen, Zhihui Sun, Yanyan Li and Youliang Hong

A kind of apatite nanosheet-constructed porous ceramics could mediate the osteogenic differentiation of mesenchymal stem cells.